Nanoscale reorganizations of histone-like nucleoid structuring proteins in *Escherichia coli* are caused by silver nanoparticles

Meaad Alqahtany[1,2,†], Prabhat Khadka[1,†], Isabelle Niyonshuti[3,†], Venkata Rao Krishnamurthi[1], Asmaa A. Sadoon[1,4,5], Sai Divya Challapalli[1,4], Jingyi Chen[3,4,*], Yong Wang[1,2,4,*]

[1.] Department of Physics, University of Arkansas, Fayetteville, 72701, USA.
[2.] Cell and Molecular Biology Program, University of Arkansas, Fayetteville, 72701, USA.
[3.] Department of Chemistry and Biochemistry, University of Arkansas, Fayetteville, 72701, USA.
[4.] Microelectronics-Photonics Program, University of Arkansas, Fayetteville, 72701, USA.
[5.] Department of Physics, University of Thi Qar, Thi Qar, Iraq.
[†.] These authors contributed equally.
[*.] To whom correspondence should be addressed: yongwang@uark.edu (YW). Correspondence can also be addressed to chenj@uark.edu (JC).

Abstract

Silver nanoparticles (AgNPs) and ions (Ag^+) have recently gained broad attention due to their antimicrobial effects against bacteria and other microbes. In this work, we demonstrate the use of super-resolution fluorescence microscopy for investigating and quantifying the antimicrobial effect of AgNPs at the molecular level. We found that subjecting *Escherichia coli* (*E. coli*) bacteria to AgNPs led to nanoscale reorganization of histone-like nucleoid structuring (H-NS) proteins, an essential nucleoid associated protein in bacteria. We observed that H-NS proteins formed denser and larger clusters at the center of the bacteria after exposure to AgNPs. We quantified the spatial reorganizations of H-NS proteins by examining the changes of various spatial parameters, including the inter-molecular distances and molecular densities. Clustering analysis based on Voronoi-tessellation were also performed to characterize the change of H-NS proteins' clustering behavior. We found that AgNP-treatment led to an increase in the fraction of H-NS proteins forming clusters. Similar effects were observed for bacteria exposed to Ag^+ ions, suggesting that the release of Ag^+ ions plays an important role in the toxicity of AgNPs. On the other hand, we observed that AgNPs with two surface coatings showed difference in the nanoscale reorganization of H-NS proteins, indicating that particle-specific effects also contribute to the antimicrobial activities of AgNPs. Our results suggested that H-NS proteins were significantly affected by AgNPs and Ag^+ ions, which has been overlooked previously. In addition, we examined the dynamic motion of AgNPs that were attached to the surface of bacteria. We expect that the current methodology can be readily applied to broadly and quantitatively study the spatial reorganization of biological macromolecules at the scale of nanometers caused by metal nanoparticles, which are expected to shed new light on the antimicrobial mechanism of metal nanoparticles.

Keywords: super-resolution fluorescence microscopy, spatial reorganization, nanoparticle, nucleoid associated protein, quantification, Voronoi diagram

Introduction

As antibiotic resistance of bacteria has become one of the biggest threats to public health [1], alternatives to antibiotics based on noble metals, such as silver (Ag), have been attracting broad interests and attention [2,3]. Ag has long been known and used as antimicrobial agents, dating back as far as ancient Greece, the Roman Empire and Egypt [4]. In the past decades, the potent antimicrobial properties of Ag have been revisited in the form of nanoparticles (AgNPs), and it has been found that AgNPs are capable of effectively suppressing the growth of and killing bacteria [5–27]. Although advancement has been made in understanding the antimicrobial effects of AgNPs, the exact antimicrobial mechanism of AgNPs remains under debate. It is commonly accepted that antimicrobial activities of AgNPs are associated to the release of Ag^{+} ions [25,28–32]; however, the particle-specific effects of AgNPs are not fully understood. For example, Xiu et al. reported that the particle-specific effects are negligible [25], while Ivask et al. observed that the toxicity mechanism of AgNPs differs from that of Ag^{+} ions [30]. In addition, there have been proposed and reported several mechanisms of bacterial damage caused by AgNPs, including DNA condensation and subsequent malfunction, free radical generation, and loss of ATP production [28,31]. For example, DNA condensation caused by AgNPs and Ag^{+} ions was observed using transmission electron microscopy (TEM) [33] and bacterial mutant strains with deficient DNA repair systems were found to be less resistant to AgNPs compared to wild type strains [34]. Furthermore, numerous previous studies were based on the ensemble measurements of the antimicrobial effects of AgNPs and Ag^{+} ions, reporting the average behavior of many bacteria responding to Ag. Little progress has been made at the single-cell and single-molecule levels.

Compared to the condensation of DNA, which has been observed for bacteria exposed to AgNPs and Ag^{+} ions using TEM [33], the changes in the spatial distribution and organization of proteins have not been reported due to the lack of the required specificity and spatial resolution. On the other hand, the organization of proteins at the molecular level, as well as cellular responses of molecular organization to environmental changes and stresses, are of great importance for many fundamental processes in cells. For example, the organization and reorganization of FtsZ proteins are tightly coupled to the cell-division in bacteria [35–37]. Spatial reorganizations of receptors have been reported to affect immune responses in a ligand-dependent manner [38]. The spatial organization of RNA polymerase in bacteria responded to growth conditions [39,40]. Therefore, it is important to investigate how AgNPs affect the spatial organization of proteins in bacteria to understand the antimicrobial activity and mechanism of AgNPs.

Here, we report our study of applying super-resolution fluorescence microscopy [41–43] to investigate and quantify the effects of AgNPs on the spatial organization of bacterial proteins. In this work, we chose an essential protein in bacteria – histone-like nucleoid structuring (H-NS) protein – as an example. The H-NS protein was chosen due to the multimodal effects of AgNPs and Ag^{+} ions and the multiple functions of H-

NS proteins in bacteria. Although H-NS proteins serve primarily as DNA-binding proteins and universal negative regulators in bacteria [44,45], it has been reported that they modulate the synthesis and stability of RNA polymerase sigma factor (RpoS) – a central protein/regulator for general stress responses [46–48], compact DNA and cause DNA condensation [49,50], modulate the production of deoxyribonucleotides and synthesis of DNA [51], enhance the cellular defenses against reactive oxygen species (ROS) [48], act as a positive regulator of genes involved in the biogenesis of flagella [52], and regulate chemotaxis proteins and thus chemotaxis [53]. Therefore, we test the hypothesis that the spatial organization of H-NS proteins are affected by AgNPs and/or Ag^+ ions in this work.

Using super-resolution fluorescence microscopy on bacteria treated with AgNPs for various durations, we found that subjecting *E. coli* bacteria to AgNPs led to nanoscale reorganizations of H-NS proteins. For example, it was found that the inter-molecular distances between H-NS proteins, which are in the order of nanometers, decreased after treatment with AgNPs. In addition, quantitative analysis showed that H-NS proteins formed denser and larger clusters at the center of the bacteria. Similar effects were observed for bacteria exposed to Ag^+ ions, suggesting that the release of Ag^+ ions from AgNPs plays a major role in the reorganizations of H-NS proteins. On the other hand, we observed that AgNPs coated with two different polymers showed difference in the reorganization of H-NS proteins, indicating that particle-specific effects are involved in the antimicrobial activities of AgNPs. The particle-specific effects were also supported by the observation that expression level of H-NS proteins increased significantly in Ag^+-treated bacteria but not in AgNP-treated ones. Furthermore, for the first time, we examined the dynamic motion of AgNPs attached to the surface of bacteria. We expect that the current work forms a new methodology readily applicable for studying the antimicrobial activity and molecular mechanism of metal nanoparticles.

Materials and Methods

Synthesis and characterization of AgNPs

Synthesis of polyvinylpyrrolidone-capped AgNPs (PVP-AgNPs). PVP-AgNPs were synthesized *via* polyol reduction method [54]. Briefly, 50 mL of ethylene glycol (EG, J.T. Baker) was added to a 250-mL 3-neck round bottom flask and heated to 150 °C in an oil bath, following by adding 0.6 mL of 3 mM NaHS (Alfa Aesar) in EG, 5 mL of 3 mM HCl (Alfa Aesar) in EG, 12 mL of 0.25 g polyvinylpyrrolidone (PVP, M_W ~55,000, Sigma-Aldrich) in EG, and 4 mL of 282 mM CH_3COOAg (Alfa Aesar). The reaction proceeded at 150 °C for ~1 h until the absorbance peak position of reaction mixture reached ~430 nm measured by UV-vis spectrometer. The reaction was then quenched by placing the flask in the ice bath. Acetone was added to the mixture at 5:1 volume ratio and the product was collected by centrifugation. The resultant PVP-AgNPs were purified using water, collected by centrifugation, and re-suspended in water for characterization and future use.

Synthesis of polyethyleneimine-capped AgNPs (PEI-AgNPs). PEI-AgNPs were prepared using a ligand exchange process. Typically, 5 mL of 5 nM (3.0×10^{12} particles/mL) PVP-AgNPs were added to 10 mL of 500 μM PEI (M_W ~2,000, J.T. Baker) solution with 1:100,000 molar ratio of AgNP:PEI. The reaction mixture was incubated for 1 h at room temperature under magnetic stirring. After incubation, the product was purified with water twice to remove excess ligands and collected by centrifugation at 14,000 rpm for 30 min. The PEI-AgNPs were then dispersed in water for characterization and future use.

Characterization of AgNPs. Transmission electron microscopy (TEM) images were captured using a TEM microscope (JEOL JEM-1011) with an accelerating voltage of 100 kV. Particle size was measured on the TEM images using Image J. UV-vis spectra were obtained using an UV-vis spectrophotometer (Agilent Cary 50). Hydrodynamic diameter, polydispersity index (PDI), and zeta potential of the nanoparticles were measured using dynamic light scattering (DLS) (Brookhaven ZetaPALS). The concentration of Ag was determined by a flame atomic absorption spectrometer (GBC 932) or by inductively coupled plasma mass spectrometry (ICP-MS) (Thermo Scientific iCap Quadrupole mass spectrometer).

Preparation of solutions of Ag^+ ions

Solutions of Ag^+ ions used in this study were prepared from $AgNO_3$ salt (Alfa Aesar), which was dissolved in ultrapure water (> 17.5 MΩ) to reach a stock concentration of 100 mM. The stock solution was sterilized by filtering through 0.22 μm cellulose filters. The concentration of Ag^+ ions in the aqueous stock was measured and confirmed using atomic absorption spectroscopy (GBC 932). The stock solutions were shielded from light by aluminum foil and stored at 4 °C for use within one week.

Bacterial strain, growth and fixation

An *E. coli* strain expressing fluorescent H-NS protein was used in this study (a gift from Dr. Milstein and Dr. Navarre [55]). Briefly, the strain was obtained by transforming a K12-derived *E. coli* strain without the *hns* gene [56] with a plasmid encoding H-NS protein fused to mEos3.2 fluorescent protein with a FLAG tag [55]. In addition, a linker of GSAGSAAGSGEF between mEos3.2 and H-NS was inserted. This strain is referred to as $K12\Delta^{hns}$/pHNS-mEos3.2C1 in this study.

The *E. coli* bacteria ($K12\Delta^{hns}$/pHNS-mEos3.2C1) were grown at 37 °C overnight in defined M9GTC medium (M9 minimal medium with 1% glucose, 0.01% thiamine, 0.1% casamino acids) [57,58], supplemented with 50 μg/mL kanamycin and 34 μg/mL chloramphenicol in a shaking incubator (250 rpm). On the second day, the overnight culture was diluted into fresh medium with a final concentration of OD_{600} = 0.05. The fresh cultures were grown again at 37 °C in the shaking incubator (250 rpm). When the OD_{600} reached ~0.3, the bacteria were either fixed directly (untreated, negative control), or treated with AgNPs or $AgNO_3$ by adding the prepared AgNPs or $AgNO_3$ stock solutions into the bacterial cultures directly. In this study, the final concentrations of AgNPs and Ag^+ ions were 40 μg/mL and 1 μg/mL (10 μM), respectively. The treated bacteria were incubated at 37 °C in the shaking incubator (250 rpm) for up to 12 hours, followed by cell fixation. Fixation of bacteria was done by adding 37% formaldehyde directly to the bacterial cultures such that the final concentration reached 3.7%, followed by incubation for 30 minutes at room temperature with orbital shaking. The bacterial cells were harvested by centrifugation at 1000g for 15 minutes at room temperature, followed by removal of the supernatant. The collected samples were washed for three times by resuspension in phosphate-buffered saline (PBS), centrifugation, and removal of supernatant. The final samples were resuspended in 1 mL PBS, wrapped with aluminum foil, stored on a nutator, and imaged by super-resolution fluorescence microscopy within 3 days.

Super-resolution fluorescence microscopy

The prepared bacteria (expressing H-NS fused to mEos3.2) were diluted by a factor of 2 – 5 in PBS to reach a reasonable density for imaging. Ten μL of the diluted samples were transferred to 5×5 mm^2 agarose pads [59,60] (~1 mm thick, 3%, prepared with PBS) so that the solutions covered the flat surfaces of the agarose pads. The samples were incubated in dark at room temperature for 20-40 min, allowing evaporation of solution and absorption and mounting of bacteria to the agarose pads. Then the agarose pads were flipped and attached to cleaned coverslips, followed by constructing chambers by sandwiching rubber o-rings between the coverslips and microscope slides. The chamber was sealed using epoxy glue and incubated at room temperature for 30-60 min in dark before imaging.

The super-resolution fluorescence microscope used in this study was home-built based on an Olympus IX-73 inverted microscope equipped with an Olympus TIRF 100X N.A.=1.49 oil immersion objective, a multi-color laser bank (iChrome MLE, Toptica Photonics AG) and an EMCCD camera (Andor, MA). The microscope and data acquisition were controlled by Micro-Manager [61]. The 405 nm and 532 nm lasers from the laser bank were used to activate and excite H-NS-mEos3.2 fusion proteins in the bacteria [41,62]. Emissions from the fluorescent proteins were collected by the objective and imaged on the EMCCD camera. The effective pixel size of acquired images was 160 nm. The resulting movies (typically ~30 fps, 20,000 frames) were analyzed with RapidStorm [63], generating localizations of H-NS proteins. The localizations that appeared in adjacent frames and within 10 nm to each other were regrouped as a single molecule [64]. The spots that were too dim, too wide, or too narrow, were rejected, while the spots that survived the criteria were further corrected for drift using a mean cross-correlation algorithm [65], and then used for generating reconstructed super-resolved images [58] and for quantitative analysis as described below.

Molecular quantification and clustering analysis of H-NS localizations

The localizations of H-NS molecules on each super-resolved image were first segmented manually into individual bacteria. The following analysis and quantification on the spatial organization of H-NS localizations were performed on the cellular basis. For each sample, 100 to 300 cells were used.

Voronoi-based quantification and clustering analysis were performed using custom-written MATLAB programs following Levet et al. [66] Briefly, the localizations of H-NS proteins in each bacterium were segmented using Voronoi tessellation [66]. The resultant Voronoi diagrams contain the information of polygons of each molecule as well as their neighboring polygons/molecules. Once the Voronoi diagrams were constructed, we calculated various parameters [66], such as the number of neighbors N_{p_i} of H-NS protein p_i, the density at protein p_i, $\rho(p_i) = \frac{1+N_{p_i}}{A_{p_i}+\sum_{p_j} A_{p_j}}$, and the distance between neighboring H-NS proteins $d(p_i, p_j) = \sqrt{\left(x_i - x_j\right)^2 + \left(y_i - y_j\right)^2}$ where (x_i, y_i) and (x_j, y_j) are the coordinates of proteins

p_i and p_j, A_{p_i} is the area of the polygonal region occupied by protein p_i. In addition, the mean inter-neighbor distances, $\Delta_{ave}(p_i) = \sum_{p_j} d(p_i, p_j) / N_{p_i}$, were estimated. All the H-NS molecules with a local density $\rho(p_i)$ above a threshold ρ_{th} were selected as candidate molecules of clusters, and neighboring candidates were merged to form clusters [66], followed by quantifying the size of the identified clusters and estimating the fraction of H-NS proteins forming clusters in each cell.

Single-particle tracking of AgNPs on bacterial surface

The bacterial samples were prepared the same as in the experiments for super-resolution fluorescence microscopy. However, a sub-movie containing a single bacterium with most of mEos3.2 fluorescent proteins photobleached was cropped out (Movie S1) for single-particle tracking (SPT) analysis using trackpy, a python-based particle-tracking toolkit [67]. The identified particles were linked into trajectory using provided functions in trackpy, with a search range of 5 pixels and a memory of 1. The individual mean-square-displacements (MSDs) were calculated using trackpy [67].

Results and Discussions

Synthesis and characterization of AgNPs

The PVP-AgNPs were synthesized through the established polyol method [54] as described above, while the PEI-AgNPs were prepared by a ligand exchange process as illustrated in Fig. 1A. The UV-vis spectra recorded before and after the ligand exchange process shows a 20 nm blue shift in the localized surface plasmon resonance (LSPR) peak of AgNPs from 425 nm for the PVP-AgNPs to 405 nm for the PEI-AgNPs (Fig. 1B). In addition to the peak shift, a weak, but broad band centered at ~495 nm arises in the spectrum of the PEI-AgNPs, possibly due to a small amount of particle aggregation. The size of the PVP-AgNPs was measured based on the TEM image (Fig. 1C), having an average edge length of 37.6 ± 4.0 nm. After the ligand-exchange process, the resultant PEI-AgNPs were found to slightly decrease in size (35.2 ± 3.1 nm) and change in shape (truncated cubes or cubes with round corners) as indicated in the TEM image in Fig. 1D. The morphological change agrees with the observed LSPR blue shift of the PEI-AgNPs compared to PVP-AgNPs because truncated particles could shift the LSPR to shorter wavelength compared to their counterparts with sharp corners [68]. The hydrodynamic diameter of the PVP-AgNPs was measured to be 112.2 nm on average with PDI of 0.21. The PVP-AgNPs were negatively charged with zeta potential of -39.4 ± 1.37 mV. The hydrodynamic diameter of the PEI-AgNPs slightly increased to 126.2 nm with a higher PDI of 0.23, perhaps due to the presence of particle aggregation. The zeta potential of PEI-AgNPs was measured to be $+15.68 \pm 1.80$ mV at pH = 7, indicative of a positively charged surface, and thus confirming a successful surface ligand exchange from PVP to PEI.

Spatial reorganization of H-NS proteins caused by AgNPs

The distribution and organization of H-NS proteins inside *E. coli* bacteria were examined using photoactivated localization microscopy (PALM) [41], with a bacterial strain [55] expressing H-NS proteins fused to mEos3.2 fluorescent proteins [62]. The fusion proteins, H-NS-mEos3.2, are fluorescent and photoactivable, allowing us to perform super-resolution fluorescence imaging. We achieved a localization precision of ~10 nm for localizing individual H-NS proteins ($\sigma_x = 9.9 \pm 2.7$ nm, $\sigma_y = 9.3 \pm 2.8$ nm, Fig. S1), equivalent to a resolution of ~23 nm. In the absence of AgNPs, we observed that H-NS proteins were organized as small clusters inside the bacteria (Fig. 2A, 2G, 2M and 2S), consistent with previously reported observations without any treatments [55,69].

When subjecting the bacteria to PVP-AgNPs at a final concentration of 40 µg/mL, changes in the spatial organization of the H-NS proteins in bacteria were observed as the treatment time increased, as shown in Fig. 2B-2L. Three major changes were observed. First, the H-NS proteins appeared brighter in the super-resolved images at longer treatment times. The enhancement in the brightness became obvious after four hours (Fig. 2E and 2F *vs*. Fig. 2A). Second, we observed that the clustering of H-NS proteins changed from small clusters (Fig. 2A and 2G) to large aggregates at the centers of the cells after four hours (Fig. 2E, 2F, and 2J-2L). Third, the H-NS occupied area became shorter at longer treatment times (Fig. 2J-2L *vs*. 2G). We also examined the bacteria treated with PEI-AgNPs at the same final concentration (40 µg/mL), and observed qualitatively similar results (Fig. 2N-2X).

To quantify the observed spatial reorganization of H-NS proteins in the super-resolved images (Fig. 2), we performed analysis based on Voronoi diagrams [66]. Briefly, we used Voronoi segmentation to divide the space into a number of polygonal regions, where each H-NS protein, p_i, occupies a polygon (with an area of A_{p_i}), as shown in Fig. S2A and S2B. The Voronoi segmentation also identified neighboring proteins, which share polygonal edges (Fig. S2A and S2B). We then computed the inter-molecular distances between neighbors [66], $d(p_i, p_j) = \sqrt{(x_i - x_j)^2 + (y_i - y_j)^2}$ where (x_i, y_i) and (x_j, y_j) are the coordinates (i.e., localizations) of H-NS proteins p_i and p_j, respectively. We examined the distributions of the occupied area of individual proteins (i.e., molecular area, A_p) and the mean inter-neighbor distances, $\mathit{\Delta}_{ave}(p_i) = \sum_{p_j} d(p_i, p_j) / N_{p_i}$, where p_j is a neighbor of p_i, and N_{p_i} is the number of neighbors of p_i. As shown in Fig. 3A and 3B, we observed that both Δ_{ave} and A_p showed log-normal distributions and that the peaks of the distributions shifted to the left (i.e., smaller values) as the treatment time with PVP-AgNPs increased. For the bacteria treated with PEI-AgNPs, similar changes in the distributions of Δ_{ave} and A_0 were observed (Fig. 3D and 3E). The decreases in both Δ_{ave} and A_0 caused by AgNPs suggested an increase in the molecular density – the local densities at the H-NS molecules, which was defined as $\rho(p_i) = \frac{1+N_{p_i}}{A_{p_i}+\sum_{p_j} A_{p_j}}$ [66]. As shown in Fig. 3C (PVP-AgNPs) and 3F (PEI-AgNPs), the distributions of the molecular density, which again showed log-normal distributions, indeed shifted to larger values after the bacteria were subjected to AgNPs for longer period of time.

We examined the horizontal translations of the distributions of the three molecular parameters (Δ_{ave}, A_p and ρ). Note that, as the distributions of the three molecular parameters were log-normal, we first converted them to their log-values (i.e., $\log_{10} \Delta_{ave}$, $\log_{10} A_p$, and $\log_{10} \rho$), from the averages of which the centers of the distributions (Fig. 3A-3F) were estimated ($\overline{\log_{10}\Delta_{ave}}$, $\overline{\log_{10}A_p}$, and $\overline{\log_{10}\rho}$). Then these average values were used to estimate the "averages" of the three molecular parameters ($\overline{\Delta_{ave}} = 10^{\overline{\log_{10}\Delta_{ave}}}$, $\overline{A_p} = 10^{\overline{\log_{10}A_p}}$, and $\bar{\rho} = 10^{\overline{\log_{10}\rho}}$). To assess the errors, we first evaluated the standard errors of the means (SEM) of the log-values (i.e., $\sigma_{\log_{10}\Delta_{ave}}$, $\sigma_{\log_{10}A_p}$, $\sigma_{\log_{10}\Delta_{ave}}$), and then estimated the errors of the "averages" using the error propagation formula (e.g.., $\sigma_{\Delta_{ave}} = \Delta_{ave} \cdot \ln 10 \cdot \sigma_{\log_{10}\Delta_{ave}}$). We observed clear decreases for the inter-neighbor distances Δ_{ave} and the areas of single molecules A_0, but an increase for the molecular density ρ. For direct comparisons, we normalized the "average" values to the untreated samples (e.g., $\gamma_{\Delta_{ave}} = \frac{\overline{\Delta_{ave}}(treated)}{\overline{\Delta_{ave}}(untreated)}$), which were shown in Fig. 3G-3I. For example, we found that, after treatment with PVP-AgNPs, the mean inter-neighbor distance Δ_{ave} decreased by 7% in 4 hours and 10% in 12 hours (Fig. 3G, blue circles), while the molecular area A_p decreased by 14% in 4 hours and 20% in 12 hours (Fig. 3H, blue circles). For bacteria treated with PEI-AgNPs, we observed that the mean inter-neighbor distance Δ_{ave} decreased by 15% in 4 hours and 35% in 12 hours (Fig. 3G, red squares), while the molecular area A_p decreased by 29% in 4 hours and 59% in 12 hours (Fig. 3H, red squares). For the molecular density ρ, we observed increases of 26% and 167% in 12 hours for bacteria treated with PVP-AgNPs and PEI-AgNPs, respectively (Fig. 3I). We note that the changes in all the three molecular parameters were more significant for bacteria treated with PEI-AgNPs than those treated with PVP-AgNPs.

To examine the changes in the clustering behavior of H-NS proteins after treatment with AgNPs, we identified the clusters of H-NS proteins from the Voronoi diagrams [66]. Briefly, H-NS molecules $\{p_i\}$ with a local density $\rho(p_i)$ above a threshold ρ_{th} were selected as candidate clustering molecules, followed by merging neighboring candidates to form clusters. The threshold ρ_{th} was chosen such that $\rho_{th} = 2 \times \rho_u$ where ρ_u is the average density for a reference distribution that is spatially uniform, according to previous studies [66,70]. In this study, the number of detected H-NS proteins was roughly ~2000 per bacterial cell. Assuming the 2D projection of an *E. coli* is a rectangle of 2000×500 nm^2, we estimated that the reference density was in the order of $\rho_u \sim \frac{2000}{2000\times500} = 0.002\ nm^{-2}$. Therefore we chose $\rho_{th} = 0.004\ nm^{-2}$ for the clustering analysis [66]. An example of bacteria with identified clusters using this method is shown in Fig. S2C. To allow direct comparisons between untreated cells and treated ones, the same threshold was used for all the samples. After identifying clusters, we quantified the clustering behavior of H-NS proteins by three clustering parameters. The first parameter is the area of a cluster A_{cl}, defined as the area of the convex envelope of all the molecules in the cluster [71]. The second parameter is the spread of a cluster, defined by the standard deviations of the coordinates of points in the cluster, $\sigma_{cl,x}$ and $\sigma_{cl,y}$. We expect that both the area A_{cl} and the spread σ_{cl} report the size of clusters, and therefore their changes are expected to be consistent upon spatial reorganization of the molecules. The distributions of A_{cl} and $\sigma_{cl,x}$ for untreated bacteria and bacteria treated with AgNPs are shown in Fig. 4A and 4B (treated with PVP-AgNPs) and Fig. 4D and 4E (treated with PEI-AgNPs). We found that the distributions were roughly log-normal, similar to the molecular parameters (Fig. 3). However, upon exposure to AgNPs for up to 12 hours, we did not observe any significant horizontal translations in the main peaks of the distributions (Fig. 4A, 4B, 4D and 4E).

Instead, we observed second peaks emerging at higher values for the bacteria treated with PEI-AgNPs after 8 and 12 hours (Fig. 4D and 4E). The second peaks led to increases in the "average" size (Fig. 4G and 4H, red squares). For example, the area of H-NS clusters A_{cl} increased by 49% in bacteria treated with PEI-AgNPs after 12 hours (Fig. 4G), which corresponded to an increase in linear size of $\sqrt{1.49} - 1 \approx 22\%$, which was consistent with the increase in the spread of the clusters $\sigma_{cl,x}$ (~19%). For the bacteria treated with PVP-AgNPs, the second peaks were absent, although a slightly larger population at higher values was observed (Fig. 4A and 4B). The center of the second peaks were ~100 times higher than that of the main peaks. For example, the second peaks of the area of clusters A_{cl} were in the order of 10^5 nm^2, while the main peaks were centered around 10^3 nm^2 (Fig. 4D). The third clustering parameters that we examined was the fraction of H-NS proteins forming clusters in each bacterium, $\phi_{cl} = \frac{N_{cp}}{N_p}$, where N_p is the number of detected H-NS proteins in a single cell, and N_{cp} is the number of H-NS proteins that are part of clusters in the same cell. We found that ϕ_{cl} did not follow the log-normal distribution. Instead, it showed peaks in linear scale (Fig. 4C and 4F). It was observed that the peaks of ϕ_{cl} shifted to the right as the treatment time increased, indicating that more proteins formed clusters after subjecting the bacteria to AgNPs. A simple estimation showed that the average clustering fraction was more than doubled (from 26% to 66%) when the bacteria were treated with PEI-AgNPs for 12 hours compared to the untreated samples (Fig. 4F and 4I).

Spatial reorganization of H-NS proteins caused by Ag^+ ions

It is commonly accepted that the release of Ag^+ ions plays an important role in the antimicrobial effects of AgNPs [25,28–32]. To justify the effectiveness of our methodology of investigating nanoscale reorganization of proteins caused by AgNPs using super-resolution fluorescence microscopy, we further examined the effects of Ag^+ ions on the distribution and organization of H-NS proteins. We hypothesized that Ag^+ ions would cause spatial reorganization of H-NS proteins similar to AgNPs. Experiments and analysis were performed on bacteria treated with Ag^+ ions at a final concentration of 10 μM. We observed that exposing bacteria to Ag^+ ions resulted in significant reorganization of H-NS proteins in *E. coli* (Fig. 5A-5N). Similar to AgNP-treated bacteria, the H-NS proteins in Ag^+-treated bacteria appeared brighter in the super-resolved images as the treatment time increased. In addition, larger clusters of H-NS proteins emerged at longer treatments at the center of the bacteria. Quantitative analysis based on Voronoi diagrams confirmed the decrease of the mean inter-neighbor distances Δ_{ave} (Fig. 5O) and the molecular area A_p (Fig. 5P), and the increase of the molecular density ρ (Fig. 5Q). Clustering analysis showed that both the size of clusters (A_{cl} and $\sigma_{cl,x}$, as shown in Fig. 5R and 5S, respectively) and the clustering fraction ϕ_{cl} (Fig. 5T) increased after subjecting bacteria to Ag^+ ions. In addition, the second peaks of the distributions of A_{cl} and $\sigma_{cl,x}$ also emerged in Ag^+-treated bacteria, similar to the PEI-AgNP-treated bacteria. Therefore, this result validated our hypothesis and confirmed that Ag^+ ions caused nanoscale reorganization of H-NS proteins. In addition, the observed similarity in the effects of AgNPs and Ag^+ ions supports that the release of Ag^+ ions from AgNPs plays an important role in the antimicrobial activities of AgNPs.

Particle-specific effects of AgNPs on the reorganization of H-NS proteins

It has been reported that the surface properties of AgNPs contribute to the antimicrobial effectiveness of AgNPs [30,72,73]. Particularly, Ivask et al. observed that PEI-AgNPs were more effective than PVP-AgNPs, which was attributed to the difference in the surface charges of the nanoparticles [30]. This particle-specific effect of AgNPs was also observed in our work using super-resolution fluorescence microscopy. As shown in Fig. 2-4, although the spatial reorganizations of H-NS proteins caused by PEI-AgNPs and PVP-AgNPs were qualitatively similar, they were different quantitatively. For example, the changes in all the three molecular parameters (Δ_{ave}, A_p and ρ) were more significant for bacteria treated with PEI-AgNPs than those treated with PVP-AgNPs (Fig. 3). In addition, the changes in the clustering parameters (A_{cl}, $\sigma_{cl,x}$ and ϕ_{cl}) were more obvious for PEI-AgNP-treated bacteria than those treated with PVP-AgNPs (Fig. 4).

To further quantify the difference in the nanoscale reorganizations caused by PEI-AgNPs and PVP-AgNPs, we examined the changing rates of the dependence of reorganization (i.e., γ's) on the treatment time T_{tr} (Fig. 3 and 4), which were obtained by fitting the data with a simple line, $\gamma = k \cdot T_{tr} + 1$ and taking the absolute value of the slope $|k|$. Note that an intercept of 1 was used as the untreated samples (i.e., $T_{tr} = 0$) should give $\gamma = 1$. As shown in Fig. 6, the changing rates $|k|$ for PEI-AgNP-treated bacteria were consistently higher than those for PVP-AgNPs treated bacteria. As a result, our data is consistent with the previous reports [30], justifying the effectiveness of our methodology of using super-resolution fluorescence microscopy and confirming the particle-specific effects of the antimicrobial activities of AgNPs.

Dynamic motion of AgNPs on bacterial surface

The interactions between AgNPs and the bacterial surface are important for the cytotoxicity of AgNPs. For example, TEM images of *S. aureus* and *E. coli* showed evidence that AgNPs were present on the cell wall and membrane of the bacteria, in addition to the cytoplasm and nucleoid [74–76]. In addition, Ivask et al. observed that AgNPs adhered to the bacterial surface of *E. coli* using atomic force microscopy (AFM) and, more importantly, that PEI-AgNPs were more effective than PVP-AgNPs in the adherence to the bacterial surface [30]. Following these exciting progresses, an interesting question is how the adhered AgNPs move dynamically on the surface of the bacteria, which has not been investigated and remains unclear. To address this question, we applied fluorescence-based single-particle tracking (SPT) to examine the dynamic motion of AgNPs on the bacterial surface. We note that, although the fluorescence spectrum of AgNPs showed a broad peak around 400-500 nm when excited at 350 nm (Fig. S3A), it was possible to image the AgNPs using our fluorescence microscope with an excitation at 532 nm and an emission window around 585 nm. Figure S3B shows a fluorescence image of AgNPs in water immobilized on a coverslip; while no fluorescent spots were observed for water without AgNPs (Fig. S3C). On the other hand, we observed the fluorescence of AgNPs was much lower than the mEos3.2 fluorescent proteins (Fig. S3D-S3F). Therefore, it was required to photobleach the fluorescent proteins before tracking the motion of the AgNP (Fig. S3D-S3F).

Movie S1 shows the dynamic motion of a single AgNP on the surface of a bacterium. The corresponding bright-field image of this bacterium (Fig. 7A) showed that the length of the cell was ~1.4 µm, shorter than normal *E. coli* bacteria [77,78]. This observation was consistent with previous studies [79]. After photobleaching the mEos3.2 proteins inside the bacterium, the fluorescent spot of the AgNP was clearly observed (Fig. 7B). By performing single-molecule localization as in super-resolution fluorescence microscopy [41–43,80–82], we reconstructed the super-resolved image for the AgNP (Fig. 7C) from 4500 frames of the movie (Movie S1). The super-resolved image showed that the trail of an AgNP appeared in a short rod shape that appeared at the periphery of the bacterium, confirming the attachment of this AgNP on the bacterial surface. In addition, from the localizations of this AgNP, we obtained its moving/diffusing trajectories using standard automated algorithms and tools [40,83–85] such as trackpy [67]. Plotting the trajectories of the AgNP on top of the brightfield image of the bacterium confirmed again that the AgNP moved at the surface of the bacterium (Fig. 7D). It is noted that both the super-resolved image and the trajectories (Fig. 7C and 7D) showed a band, instead of a narrow line, around the periphery of the bacterium for the AgNP, presumably due to the diffusion of the AgNP in z-direction. In addition, three trajectories were automatedly identified by trackpy for this AgNP, instead of a single trajectory, presumably due to again the AgNP moving out of focus or blinking temporarily. On the other hand, if the AgNP moved out of focus too far, its intensity would fell below the set thresholds during trackpy or super-resolution analysis, resulting in a "hollow" area inside the bacterium, similar to the super-resolved results of high-copy-number plasmids in bacteria [58]. Examining the trajectories in more details showed that the AgNP moved diffusively first and then got immobilized at the end of the movie (Fig. 7D), which can be seen clearly in the plots of position of the AgNP *vs.* frame number (Fig. 7E). From the trajectories, the mean-square-displacements (MSD) were calculated, showing slopes of 1 in the log-log scale at short time scales (<0.4 s, Fig. 7F) and indicating a Brownian diffusion. At longer time scales (0.5-5 s, Fig. 7F), the MSD curves deviates from the Brownian diffusion, bending down and suggesting a sub-diffusion [40,85–88]. We note that the deviation is unlikely due to poor statistics as the length of each trajectory is >1000 frames (i.e., >45 s, Fig. 7E). To our knowledge, this result presents the first study on the dynamic motion of AgNPs attached to the bacterial surface. The observed sub-diffusion of the attached AgNP is qualitatively consistent with the sub-diffusion of membrane proteins of bacteria reported previously [17], providing evidence to support the previous suggestion that AgNPs attach to membrane proteins, which contain cysteines and thus thiol groups that interact with Ag [30,72,73].

Conclusions

To summarize, we used quantitative super-resolution fluorescence microscopy to study the response of bacteria to treatment with AgNPs or Ag^+ ions at the molecular level by examining the nanoscale reorganization of H-NS proteins in *E. coli*. We found that subjecting *E. coli* bacteria to both PVP-AgNPs and PEI-AgNPs caused denser and larger clusters of H-NS proteins. The degree of the nanoscale reorganizations was dependent on the treatment time. We quantified the nanoscale reorganizations of H-NS proteins using three molecular parameters (the mean inter-neighbor distance Δ_{ave}, the molecular area

A_p, and the molecular density ρ) and three clustering parameters (the area of clusters A_{cl}, the spread of clusters $\sigma_{cl,x}$, and the fraction of H-NS proteins forming clusters ϕ_{cl}), which were based on Voronoi-tessellation [66]. We also characterized the changing rates of these parameters from their dependence on the treatment time. Similar effects were observed for bacteria exposed to Ag^+ ions, suggesting that the release of Ag^+ ions plays an important role in the toxicity of AgNPs. On the other hand, we observed that PEI-AgNPs showed larger reorganizations of H-NS proteins and higher changing rates of those molecular and clustering parameters compared to PVP-AgNPs at the same concentration, indicating that particle-specific effects also contribute to the antimicrobial activities of AgNPs. Lastly, we examined the dynamic motion of AgNPs attached to the surface of bacteria, for the first time, and quantified the diffusive behavior of the AgNP using mean-square displacement (MSD).

Six parameters based on Voronoi tessellation were chosen in this work for quantifying the nanoscale reorganization of H-NS proteins caused by AgNPs. It is worthwhile to point out that, due to the advantage of super-resolution fluorescence microscopy that the positions (coordinates) of the proteins of interest are acquired, many other quantitative parameters or functions could be exploited, including the current parameters at higher orders [66]. In addition, other quantitative analysis of the spatial organization of molecules, such as Ripley's K function [89,90] and nearest-neighbor functions [91–94] can be used.

Our results suggested that H-NS proteins were significantly affected by both AgNPs and Ag^+ ions, which has been overlooked previously. Considering the central and regulatory functions of H-NS proteins in bacteria [44–53], it is not surprising that AgNPs and Ag^+ ions would affect various cellular processes that are regulated, directly or indirectly, by H-NS proteins. On the other hand, our work brings up new questions. For example, it is unclear whether the previously observed DNA condensation [33] caused by Ag^+ ions and AgNPs is a result of, or a reason for, the spatial reorganization of H-NS proteins. Our work opens a new avenue and introduces new angles for understanding the antimicrobial activity and mechanism of AgNPs.

Although it has been known that AgNPs attach to and interact with the cell wall and membrane of bacteria for their antimicrobial activities [30,74–76], our study provided the first dynamic study on the motion and diffusion of AgNPs on the bacterial surface. While this result advanced our understanding on the AgNP-membrane interactions, more importantly, new questions were raised. For example, it is not clear why the AgNP got immobilized on the bacterial surface at the end. Possible reasons include membrane damage, changes of membrane components, and formation multiple attachment points. Future experiments involving multi-color imaging of both AgNPs and bacterial membrane would help to address the newly-arising questions.

The current work provides a methodological framework for quantitatively studying the antimicrobial activity and mechanism of metal nanoparticles at the molecular level in general. As H-NS is one major member of the >12 nucleoid-associated proteins (NAPs) in gram-negative bacteria [44,95], it would be interesting to examine how the other NAPs are affected by Ag^+ ions and AgNPs. In addition, the response of 4159 *E. coli* single nonessential gene mutant strains were investigated in terms of toxicity of Ag^+ ions and AgNPs, and groups of genes were identified to be sensitive to Ag^+ ions and/or AgNPs with various coatings in a previous work by Ivask et al. [30] It would be interesting to apply the method from this work for quantitative, detailed, molecular studies of the individual sensitive genes identified from Ivask et al.'s work [30], and to compare the differences in the molecular responses to Ag^+ ions *vs.* AgNPs. We expect that the method in this work will provide quantitative, previously inaccessible information for understanding the antimicrobial activities and mechanism of Ag^+ ions and AgNPs.

Conflicts of interest

There are no conflicts to declare.

Acknowledgements

We thank Dr. Joshua N. Milstein for the generous gift of the E. coli strain expressing mEos3.2-HNS fusion proteins. This work was supported by the University of Arkansas start-up supports to Y.W., the Arkansas Biosciences Institute (Grant No. ABI-0189, No. ABI-0226, and No. ABI-0277 to Y.W.), and the National Science Foundation (Grant No. 1826642 to Y.W. and J.C.). This work was partially supported by the Center for Advanced Surface Engineering, under the National Science Foundation Grant No. OIA-1457888 and the Arkansas EPSCoR Program, ASSET III. ICP-MS measurements were carried out at the Arkansas Mass Spectrometry facility, which is supported by the Arkansas Biosciences Institute. M.Q. was financially supported by Saudi Arabian Cultural Mission program. We are also grateful for supports from the Arkansas High Performance Computing Center (AHPCC), which is funded in part by the National Science Foundation (Grants No. 0722625, 0959124, 0963249, 0918970) and the Arkansas Science and Technology Authority.

Notes and References

[1] World Health Organization 2014 *World Health statistics 2014*

[2] François B, Jafri H S and Bonten M 2016 Alternatives to antibiotics *Intensive Care Med* **42** 2034–6

[3] Allen H K, Trachsel J, Looft T and Casey T A 2014 Finding alternatives to antibiotics *Annals Of The New York Academy Of Sciences* **1323** 91–100

[4] Alexander J W 2009 History of the Medical Use of Silver *Surg. Infect.* **10** 289–92

[5] Agnihotri S, Mukherji S and Mukherji S 2014 Size-controlled silver nanoparticles synthesized over the range 5–100 nm using the same protocol and their antibacterial efficacy *RSC Adv* **4** 3974–83

[6] Bao H, Yu X, Xu C, Li X, Li Z, Wei D and Liu Y 2015 New toxicity mechanism of silver nanoparticles: Promoting apoptosis and inhibiting proliferation *PLoS ONE* **10** 1–10

[7] Bresee J, Maier K E, Boncella A E, Melander C and Feldheim D L 2011 Growth inhibition of staphylococcus aureus by mixed monolayer gold nanoparticles *Small* **7** 2027–31

[8] Chatterjee A K, Chakraborty R and Basu T 2014 Mechanism of antibacterial activity of copper nanoparticles. *Nanotechnology* **25** 135101–135101

[9] Chowdhury M N K, Beg M D H, Khan M R and Mina M F 2013 Synthesis of copper nanoparticles and their antimicrobial performances in natural fibres *Mater. Lett.* **98** 26–9

[10] Cui Y, Zhao Y, Tian Y, Zhang W, Lu X and Jiang X 2012 The molecular mechanism of action of bactericidal gold nanoparticles on Escherichia coli *Biomaterials* **33** 2327–33

[11] Fukuoka T, Yamaguchi A, Hara R, Matsumoto T, Utsumi Y and Mori Y 2015 Application of gold nanoparticle self-assemblies to unclonable anti-counterfeiting technology *2015 International Conference on Electronic Packaging and iMAPS All Asia Conference (ICEP-IAAC)* (IEEE) pp 432–5

[12] Geethalakshmi R and Sarada D V L 2013 Characterization and antimicrobial activity of gold and silver nanoparticles synthesized using saponin isolated from Trianthema decandra L. *Ind. Crops Prod.* **51** 107–15

[13] Kim J S, Kuk E, Yu K N, Kim J-H, Park S J, Lee H J, Kim S H, Park Y K, Park Y H, Hwang C-Y, Kim Y-K, Lee Y-S, Jeong D H and Cho M-H 2007 Antimicrobial effects of silver nanoparticles *Nanomedicine Nanotechnol. Biol. Med.* **3** 95–101

[14] Le Ouay B and Stellacci F 2015 Antibacterial activity of silver nanoparticles: A surface science insight *Nano Today* **10** 339–54

[15] Li X, Robinson S M, Gupta A, Saha K, Jiang Z, Moyano D F, Sahar A, Riley M A and Rotello V M 2014 Functional Gold Nanoparticles as Potent Antimicrobial Agents against Multi-Drug-Resistant Bacteria *ACS Nano* **8** 10682–6

[16] Maiti S, Krishnan D, Barman G, Ghosh S K and Laha J K 2014 Antimicrobial activities of silver nanoparticles synthesized from Lycopersicon esculentum extract *J. Anal. Sci. Technol.* **5** 40–40

[17] Meeker D, Jenkins S V, Miller E K, Beenken K, Loughran A, Powless A, Muldoon T, Galanzha E I, Zharov V, Smeltzer M S and Chen J 2016 Synergistic Photothermal and Antibiotic Killing of Biofilm-associated Staphylococcus aureus using Targeted, Antibiotic-loaded Gold Nanoconstructs *ACS Infect. Dis.* acsinfecdis.5b00117-acsinfecdis.5b00117

[18] Pal S, Tak Y K and Song J M 2007 Does the Antibacterial Activity of Silver Nanoparticles Depend on the Shape of the Nanoparticle? A Study of the Gram-Negative Bacterium Escherichia coli *Appl. Environ. Microbiol.* **73** 1712–20

[19] Raffi M, Mehrwan S, Bhatti T M, Akhter J I, Hameed A, Yawar W and ul Hasan M M 2010 Investigations into the antibacterial behavior of copper nanoparticles against Escherichia coli *Ann. Microbiol.* **60** 75–80

[20] Ramyadevi J, Jeyasubramanian K, Marikani A, Rajakumar G and Rahuman A A 2012 Synthesis and antimicrobial activity of copper nanoparticles *Mater. Lett.* **71** 114–6

[21] Ruparelia J P, Chatterjee A K, Duttagupta S P and Mukherji S 2008 Strain specificity in antimicrobial activity of silver and copper nanoparticles *Acta Biomater.* **4** 707–16

[22] Shaalan M, Saleh M, El-Mahdy M and El-Matbouli M 2016 Recent progress in applications of nanoparticles in fish medicine: A review *Nanomedicine Nanotechnol. Biol. Med.* **12** 701–10

[23] Sondi I and Salopek-Sondi B 2004 Silver nanoparticles as antimicrobial agent: a case study on E. coli as a model for Gram-negative bacteria *J. Colloid Interface Sci.* **275** 177–82

[24] Wei Y, Chen S, Kowalczyk B, Huda S, Gray T P and Grzybowski B A 2010 Synthesis of Stable, Low-Dispersity Copper Nanoparticles and Nanorods and Their Antifungal and Catalytic Properties *J. Phys. Chem. C* **114** 15612–6

[25] Xiu Z, Zhang Q, Puppala H L, Colvin V L and Alvarez P J J 2012 Negligible particle-specific antibacterial activity of silver nanoparticles. *Nano Lett.* **12** 4271–5

[26] Zhao Y, Tian Y, Cui Y, Liu W, Ma W and Jiang X 2010 Small Molecule-Capped Gold Nanoparticles as Potent Antibacterial Agents That Target Gram-Negative Bacteria *J. Am. Chem. Soc.* **132** 12349–56

[27] Zhou Y, Kong Y, Kundu S, Cirillo J D and Liang H 2012 Antibacterial activities of gold and silver nanoparticles against Escherichia coli and bacillus Calmette-Guérin. *J. Nanobiotechnology* **10** 19–19

[28] Durán N, Durán M, de Jesus M B, Seabra A B, Fávaro W J and Nakazato G 2016 Silver nanoparticles: A new view on mechanistic aspects on antimicrobial activity *Nanomedicine: Nanotechnology, Biology and Medicine* **12** 789–99

[29] Hwang E T, Lee J H, Chae Y J, Kim Y S, Kim B C, Sang B-I and Gu M B 2008 Analysis of the Toxic Mode of Action of Silver Nanoparticles Using Stress-Specific Bioluminescent Bacteria *Small* **4** 746–50

[30] Ivask A, ElBadawy A, Kaweeteerawat C, Boren D, Fischer H, Ji Z, Chang C H, Liu R, Tolaymat T, Telesca D, Zink J I, Cohen Y, Holden P A and Godwin H A 2014 Toxicity Mechanisms in Escherichia coli Vary for Silver Nanoparticles and Differ from Ionic Silver *ACS Nano* **8** 374–86

[31] Jung W K, Koo H C, Kim K W, Shin S, Kim S H and Park Y H 2008 Antibacterial Activity and Mechanism of Action of the Silver Ion in Staphylococcus aureus and Escherichia coli *Appl. Environ. Microbiol.* **74** 2171–8

[32] Marambio-Jones C and Hoek E M V 2010 A review of the antibacterial effects of silver nanomaterials and potential implications for human health and the environment *J Nanopart Res* **12** 1531–51

[33] Feng Q L, Wu J, Chen G Q, Cui F Z, Kim T N and Kim J O 2000 A mechanistic study of the antibacterial effect of silver ions on Escherichia coli andStaphylococcus aureus *J. Biomed. Mater. Res.* **52** 662–8

[34] Radzig M A, Nadtochenko V A, Koksharova O A, Kiwi J, Lipasova V A and Khmel I A 2013 Antibacterial effects of silver nanoparticles on gram-negative bacteria: Influence on the growth and biofilms formation, mechanisms of action *Colloids and Surfaces B: Biointerfaces* **102** 300–6

[35] Xiao J and Goley E D 2016 Redefining the roles of the FtsZ-ring in bacterial cytokinesis *Current Opinion in Microbiology* **34** 90–6

[36] Fu G, Huang T, Buss J, Coltharp C, Hensel Z and Xiao J 2010 In Vivo Structure of the E. coli FtsZ-ring Revealed by Photoactivated Localization Microscopy (PALM) *PLOS ONE* **5** e12680

[37] Liu R, Liu Y, Liu S, Wang Y, Li K, Li N, Xu D and Zeng Q 2017 Three-Dimensional Superresolution Imaging of the FtsZ Ring during Cell Division of the Cyanobacterium Prochlorococcus *mBio* **8** e00657-17

[38] Bálint Š, Lopes F B and Davis D M 2018 A nanoscale reorganization of the IL-15 receptor is triggered by NKG2D in a ligand-dependent manner *Sci. Signal.* **11** eaal3606

[39] Endesfelder U, Finan K, Holden S J, Cook P R, Kapanidis A N and Heilemann M 2013 Multiscale spatial organization of RNA polymerase in escherichia coli *Biophys. J.* **105** 172–81

[40] Stracy M, Lesterlin C, Garza de Leon F, Uphoff S, Zawadzki P and Kapanidis A N 2015 Live-cell superresolution microscopy reveals the organization of RNA polymerase in the bacterial nucleoid *Proc. Natl. Acad. Sci.* **112** E4390–9

[41] Betzig E, Patterson G H, Sougrat R, Lindwasser O W, Olenych S, Bonifacino J S, Davidson M W, Lippincott-Schwartz J and Hess H F 2006 Imaging intracellular fluorescent proteins at nanometer resolution. *Science* **313** 1642–5

[42] Bates M, Huang B, Dempsey G T and Zhuang X 2007 Multicolor super-resolution imaging with photo-switchable fluorescent probes. *Science* **317** 1749–53

[43] Huang B, Wang W, Bates M and Zhuang X 2008 Three-dimensional super-resolution imaging by stochastic optical reconstruction microscopy. *Science* **319** 810–3

[44] Dorman C J 2004 H-NS: a universal regulator for a dynamic genome *Nat. Rev. Microbiol.* **2** 391–400

[45] Gao Y, Foo Y H, Winardhi R S, Tang Q, Yan J and Kenney L J 2017 Charged residues in the H-NS linker drive DNA binding and gene silencing in single cells *PNAS* **114** 12560–5

[46] Brescia C C, Kaw M K and Sledjeski D D 2004 The DNA binding protein H-NS binds to and alters the stability of RNA in vitro and in vivo *J. Mol. Biol.* **339** 505–14

[47] Zhou Y and Gottesman S 2006 Modes of Regulation of RpoS by H-NS *J. Bacteriol.* **188** 7022–5

[48] Gérard F, Dri A-M and Moreau P L 1999 Role of Escherichia coli RpoS, LexA and H-NS global regulators in metabolism and survival under aerobic, phosphate-starvation conditions *Microbiology* **145** 1547–62

[49] Dame R T, Wyman C and Goosen N 2000 H-NS mediated compaction of DNA visualised by atomic force microscopy *Nucleic Acids Res* **28** 3504–10

[50] Winardhi R S, Yan J and Kenney L J 2015 H-NS Regulates Gene Expression and Compacts the Nucleoid: Insights from Single-Molecule Experiments *Biophysical Journal* **109** 1321–9

[51] Cendra M del M, Juárez A, Madrid C and Torrents E 2013 H-NS Is a Novel Transcriptional Modulator of the Ribonucleotide Reductase Genes in Escherichia coli *J. Bacteriol.* **195** 4255–63

[52] Bertin P, Terao E, Lee E H, Lejeune P, Colson C, Danchin A and Collatz E 1994 The H-NS protein is involved in the biogenesis of flagella in Escherichia coli. *J. Bacteriol.* **176** 5537–40

[53] Wang H, Ayala J C, Benitez J A and Silva A J 2015 RNA-Seq Analysis Identifies New Genes Regulated by the Histone-Like Nucleoid Structuring Protein (H-NS) Affecting Vibrio cholerae Virulence, Stress Response and Chemotaxis *PLOS ONE* **10** e0118295

[54] Zhang Q, Li W, Wen L-P, Chen J and Xia Y 2010 Facile Synthesis of Ag Nanocubes of 30 to 70 nm in Edge Length with CF 3 COOAg as a Precursor *Chem. - Eur. J.* **16** 10234–9

[55] Mazouchi A and Milstein J N 2016 Fast Optimized Cluster Algorithm for Localizations (FOCAL): a spatial cluster analysis for super-resolved microscopy *Bioinformatics* **32** 747–54

[56] Baba T, Ara T, Hasegawa M, Takai Y, Okumura Y, Baba M, Datsenko K A, Tomita M, Wanner B L and Mori H 2006 Construction of Escherichia coli K-12 in-frame, single-gene knockout mutants: the Keio collection. *Mol. Syst. Biol.* **2** 2006.0008-2006.0008

[57] Sambrook J and Russell D W 2001 *Molecular Cloning: A Laboratory Manual* (Cold Spring Harbor Laboratory Press)

[58] Wang Y, Penkul P and Milstein J N N 2016 Quantitative Localization Microscopy Reveals a Novel Organization of a High-Copy Number Plasmid *Biophys. J.* **111** 467–79

[59] Young J W, Locke J C W, Altinok A, Rosenfeld N, Bacarian T, Swain P S, Mjolsness E and Elowitz M B 2011 Measuring single-cell gene expression dynamics in bacteria using fluorescence time-lapse microscopy. *Nat. Protoc.* **7** 80–8

[60] Skinner S O, Sepúlveda L a, Xu H and Golding I 2013 Measuring mRNA copy number in individual Escherichia coli cells using single-molecule fluorescent in situ hybridization. *Nat. Protoc.* **8** 1100–13

[61] Edelstein A, Amodaj N, Hoover K, Vale R and Stuurman N 2010 Computer Control of Microscopes Using Micro-Manager *Current Protocols in Molecular Biology* (Hoboken, NJ, USA: John Wiley & Sons, Inc.)

[62] Zhang M, Chang H, Zhang Y, Yu J, Wu L, Ji W, Chen J, Liu B, Lu J, Liu Y, Zhang J, Xu P and Xu T 2012 Rational design of true monomeric and bright photoactivatable fluorescent proteins *Nat. Methods* **9** 727–9

[63] Wolter S, Löschberger A, Holm T, Aufmkolk S, Dabauvalle M-C, Linde S V D, Sauer M and van de Linde S 2012 rapidSTORM : accurate , fast open-source software for localization microscopy orcae : online resource for community annotation of eukaryotes *Nat. Methods* **9** 1040–1

[64] Coltharp C, Kessler R P and Xiao J 2012 Accurate Construction of Photoactivated Localization Microscopy (PALM) Images for Quantitative Measurements ed M Sauer *PLoS ONE* **7** e51725–e51725

[65] Wang Y, Schnitzbauer J, Hu Z, Li X, Cheng Y, Huang Z-L and Huang B 2014 Localization events-based sample drift correction for localization microscopy with redundant cross-correlation algorithm. *Opt. Express* **22** 15982–91

[66] Levet F, Hosy E, Kechkar A, Butler C, Beghin A, Choquet D and Sibarita J-B 2015 SR-Tesseler: a method to segment and quantify localization-based super-resolution microscopy data *Nat. Methods* **12**

[67] Allan D B, Caswell T, Keim N C and van der Wel C M 2018 *trackpy: Trackpy v0.4.1* (Zenodo)

[68] Crane C C, Wang F, Li J, Tao J, Zhu Y and Chen J 2017 Synthesis of Copper–Silica Core–Shell Nanostructures with Sharp and Stable Localized Surface Plasmon Resonance *J. Phys. Chem. C* **121** 5684–92

[69] Wang S, Moffitt J R, Dempsey G T, Xie X S and Zhuang X 2014 Characterization and development of photoactivatable fluorescent proteins for single-molecule-based superresolution imaging. *Proc. Natl. Acad. Sci. U. S. A.* **111** 8452–7

[70] Andronov L, Orlov I, Lutz Y, Vonesch J-L and Klaholz B P 2016 ClusterViSu, a method for clustering of protein complexes by Voronoi tessellation in super-resolution microscopy. *Sci. Rep.* **6** 24084–24084

[71] Berg M de 2008 *Computational Geometry: Algorithms and Applications* (Springer Science & Business Media)

[72] Carlson C, Hussain S M, Schrand A M, K. Braydich-Stolle L, Hess K L, Jones R L and Schlager J J 2008 Unique Cellular Interaction of Silver Nanoparticles: Size-Dependent Generation of Reactive Oxygen Species *J. Phys. Chem. B* **112** 13608–19

[73] Oberdörster Günter, Oberdörster Eva and Oberdörster Jan 2007 Concepts of Nanoparticle Dose Metric and Response Metric *Environmental Health Perspectives* **115** A290–A290

[74] Mei L, Lu Z, Zhang W, Wu Z, Zhang X, Wang Y, Luo Y, Li C and Jia Y 2013 Bioconjugated nanoparticles for attachment and penetration into pathogenic bacteria *Biomaterials* **34** 10328–37

[75] Li W-R, Xie X-B, Shi Q-S, Zeng H-Y, OU-Yang Y-S and Chen Y-B 2010 Antibacterial activity and mechanism of silver nanoparticles on Escherichia coli *Appl Microbiol Biotechnol* **85** 1115–22

[76] Morones J R, Elechiguerra J L, Camacho A, Holt K, Kouri J B, Ramírez J T and Yacaman M J 2005 The bactericidal effect of silver nanoparticles *Nanotechnology* **16** 2346–53

[77] Tortora G J, Funke B R and Case C L 2015 *Microbiology: An Introduction* (Pearson)

[78] Moran U, Phillips R and Milo R 2010 SnapShot: Key Numbers in Biology *Cell* **141** 1262-1262.e1

[79] Gogoi S K, Gopinath P, Paul A, Ramesh A, Ghosh S S and Chattopadhyay A 2006 Green Fluorescent Protein-Expressing Escherichia coli as a Model System for Investigating the Antimicrobial Activities of Silver Nanoparticles *Langmuir* **22** 9322–8

[80] Yildiz A, Forkey J N, McKinney S a, Ha T, Goldman Y E and Selvin P R 2003 Myosin V walks hand-over-hand: single fluorophore imaging with 1.5-nm localization. *Science* **300** 2061–5

[81] Yildiz A, Tomishige M, Vale R D and Selvin P R 2004 Kinesin walks hand-over-hand. *Science* **303** 676–8

[82] Wang Y, Cai E, Sheung J, Lee S H, Teng K W and Selvin P R 2014 Fluorescence Imaging with One-nanometer Accuracy (FIONA) *J. Vis. Exp.* 1–8

[83] Crocker J C and Grier D G 1996 Methods of Digital Video Microscopy for Colloidal Studies *Journal of Colloid and Interface Science* **179** 298–310

[84] Manley S, Gillette J M, Patterson G H, Shroff H, Hess H F, Betzig E and Lippincott-Schwartz J 2008 High-density mapping of single-molecule trajectories with photoactivated localization microscopy *Nat Meth* **5** 155–7

[85] Sadoon A A and Wang Y 2018 Anomalous, non-Gaussian, viscoelastic, and age-dependent dynamics of histonelike nucleoid-structuring proteins in live Escherichia coli *Phys. Rev. E* **98** 042411

[86] Bakshi S, Siryaporn A, Goulian M and Weisshaar J C 2012 Superresolution imaging of ribosomes and RNA polymerase in live Escherichia coli cells *Mol. Microbiol.* **85** 21–38

[87] Weber S C, Spakowitz A J and Theriot J A 2010 Bacterial Chromosomal Loci Move Subdiffusively through a Viscoelastic Cytoplasm *Phys. Rev. Lett.* **104** 238102

[88] Metzler R, Jeon J-H and Cherstvy A G 2016 Non-Brownian diffusion in lipid membranes: Experiments and simulations *Biochimica et Biophysica Acta (BBA) - Biomembranes* **1858** 2451–67

[89] Ripley B D 1988 *Statistical Inference for Spatial Processes* (Cambridge: Cambridge University Press)

[90] Kiskowski M A, Hancock J F and Kenworthy A K 2009 On the Use of Ripley's K-Function and Its Derivatives to Analyze Domain Size *Biophys. J.* **97** 1095–103

[91] Jiang S, Park S, Challapalli S D, Fei J and Wang Y 2017 Robust nonparametric quantification of clustering density of molecules in single-molecule localization microscopy *PLOS ONE* **12** e0179975

[92] Diggle P J 2003 *Statistical Analysis of Spatial Point Patterns* (London; New York: Hodder Education Publishers)

[93] van Lieshout M N M and Baddeley A 1996 A non-parametric measure of spatial interaction in point patterns *Stat. Neerlandica* **50** 344–61

[94] Kerscher M, Pons-Borderia M J, Schmalzing J, Trasarti-Battistoni R, Buchert T, Martinez V J and Valdarnini R 1999 A Global Descriptor of Spatial Pattern Interaction in the Galaxy Distribution *Astrophys. J.* **513** 543–8

[95] Dillon S C and Dorman C J 2010 Bacterial nucleoid-associated proteins, nucleoid structure and gene expression *Nat Rev Micro* **8** 185–95

Figures and Figure Legends

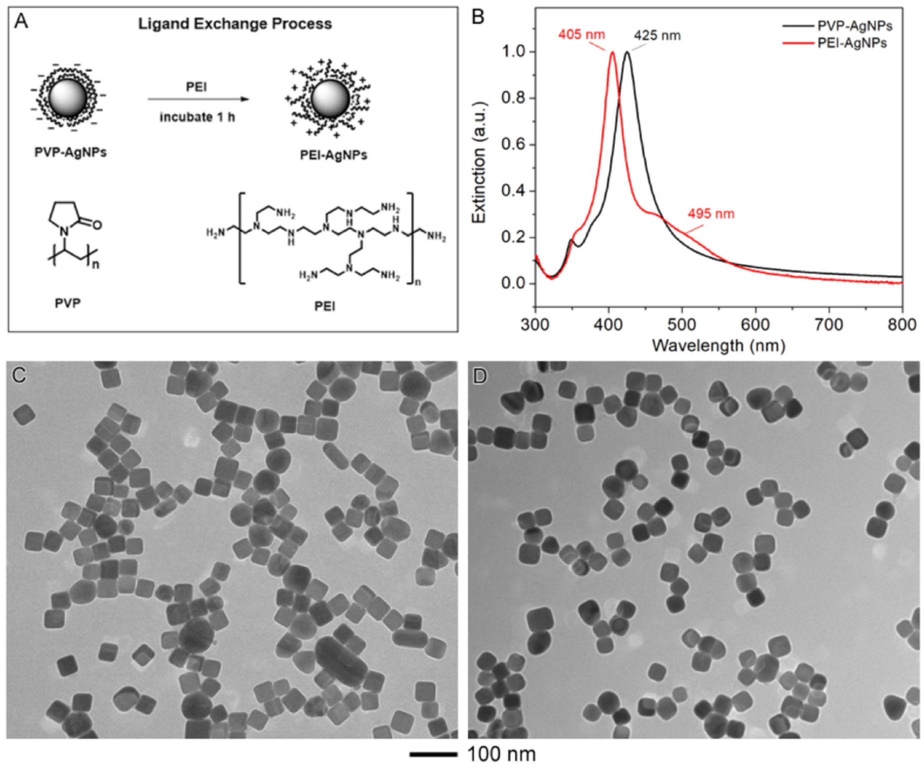

Figure 1. Synthesis and characterization of PVP-AgNPs and PEI-AgNPs. (A) Reaction scheme of PEI-AgNPs from PVP-AgNPs using a ligand exchange process. (B) Absorbance spectra of PVP-AgNPs (black) and PEI-AgNPs (red). (C) TEM characterization of PVP-AgNPs. (D) TEM characterization of PEI-AgNPs. Scale bar = 100 nm for both panels C and D.

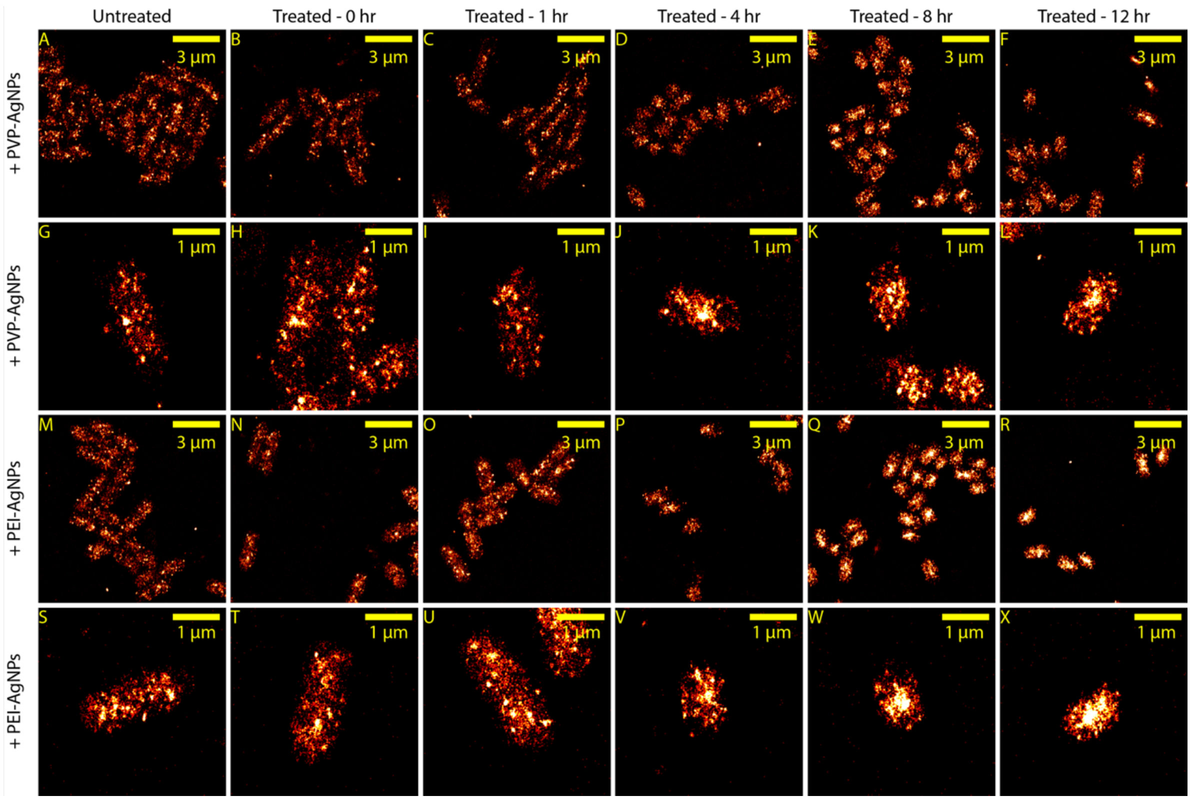

Figure 2. Super-resolved images of H-NS proteins in *E. coli* bacteria before (first column) and after (columns 2-6) subjecting bacteria to treatments with PVP-AgNPs (top two rows) and PEI-AgNPs (bottom two rows) for 0-12 hours. Row 2 and 4 are zoom-in images of single bacteria.

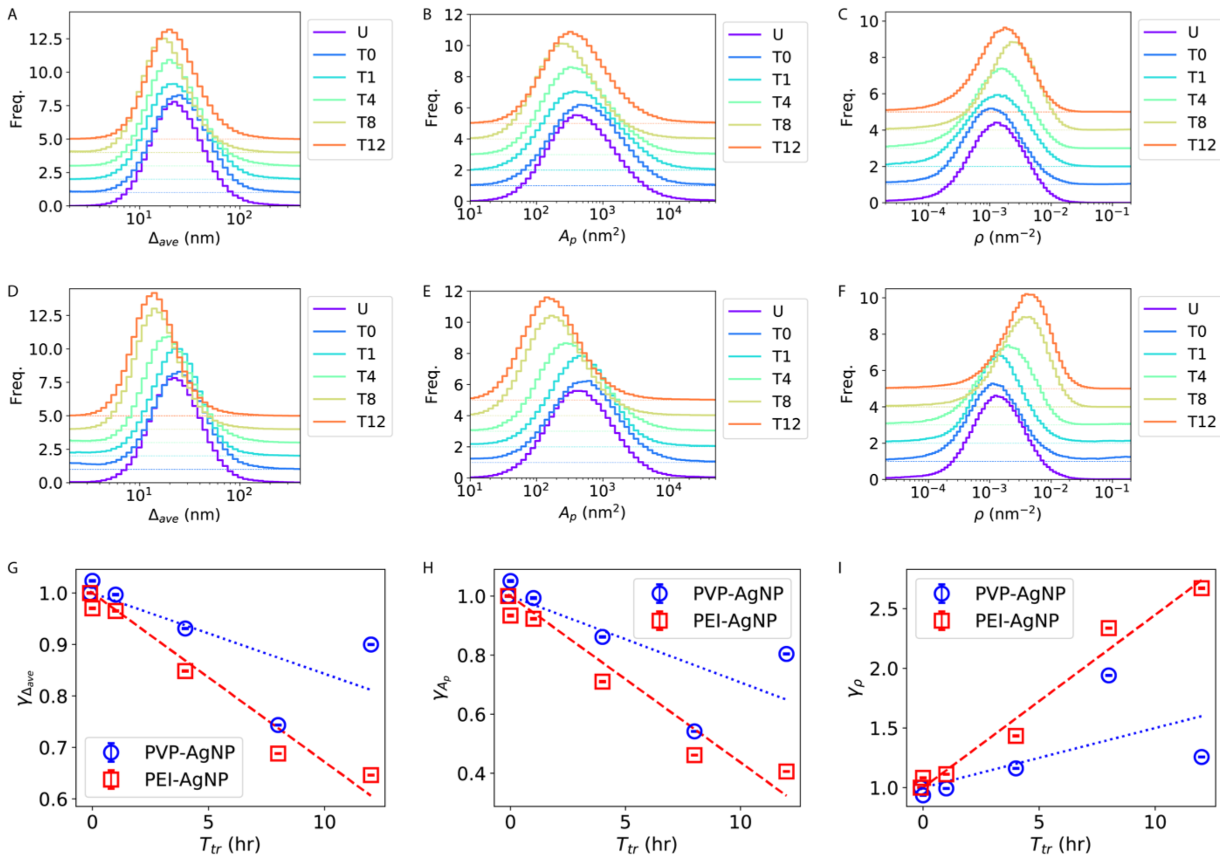

Figure 3. Nanoscale reorganization of H-NS proteins caused by AgNPs quantified by three molecular parameters: the mean inter-neighbor distances Δ_{ave}, the molecular area A_p, and the molecular density ρ. (A-C) show the distributions of the three molecular parameters for bacteria treated with PVP-AgNPs, while (D-F) show the distributions of the three molecular parameters for bacteria treated with PEI-AgNPs. The distributions in (A-F) were shifted vertically to reduce overlapping between the distributions and to facilitate the visualization of the horizontal translations of the distributions. (G-I) Dependence of the centers of the distributions of the three molecular parameters (normalized to the untreated bacteria) on treatment-time. Dashed and dotted lines are fittings.

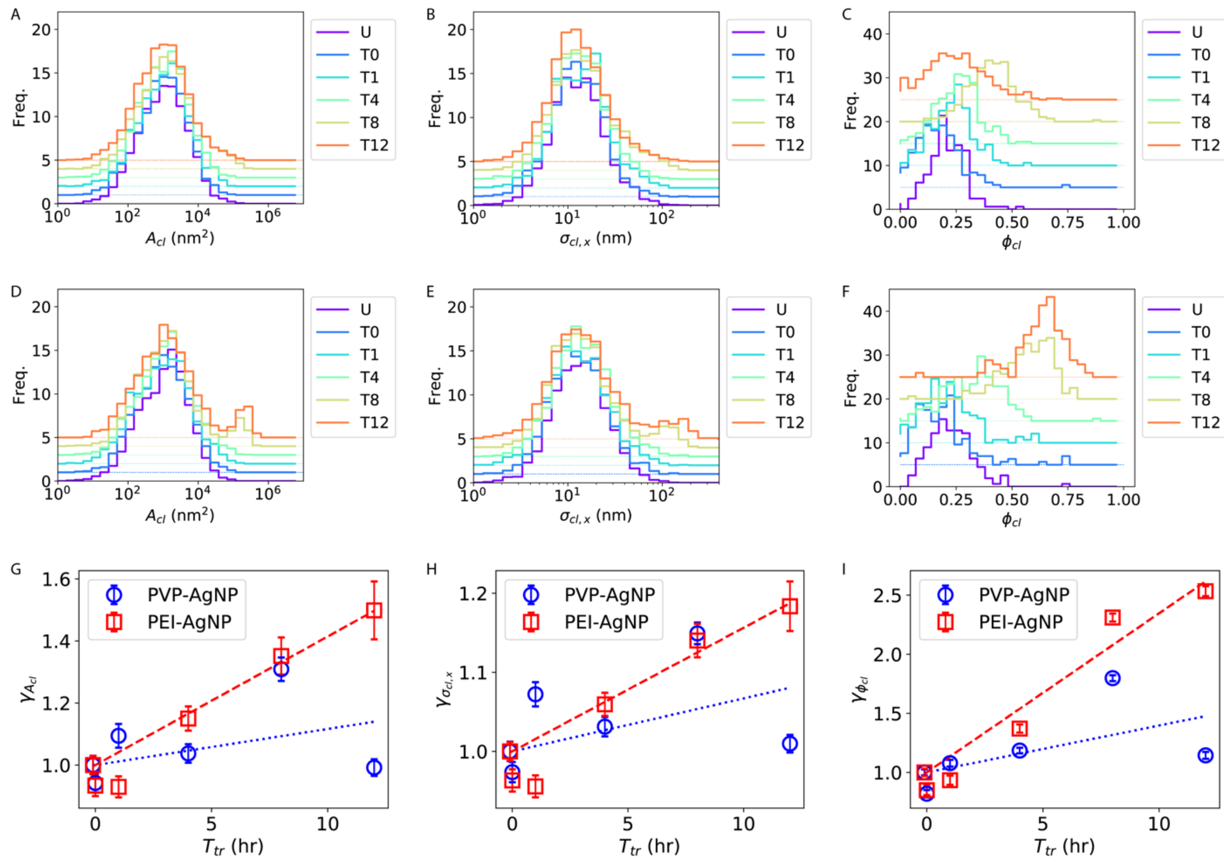

Figure 4. Nanoscale reorganization of H-NS proteins caused by AgNPs quantified by three clustering parameters: the area of clusters of H-NS proteins A_{cl}, the spread of clusters in x-direction $\sigma_{cl,x}$, and the fraction of proteins forming clusters in each bacterium ϕ_{cl}. (A-C) show the distributions of the three clustering parameters for bacteria treated with PVP-AgNPs, while (D-F) show the distributions of the three clustering parameters for bacteria treated with PEI-AgNPs. The distributions in (A-F) were shifted vertically to reduce overlapping between the distributions and to facilitate the visualization of the horizontal translations of the distributions. (G-I) Dependence of the centers of the distributions of the three clustering parameters (normalized to the untreated bacteria) on treatment-time. Dashed and dotted lines are fittings.

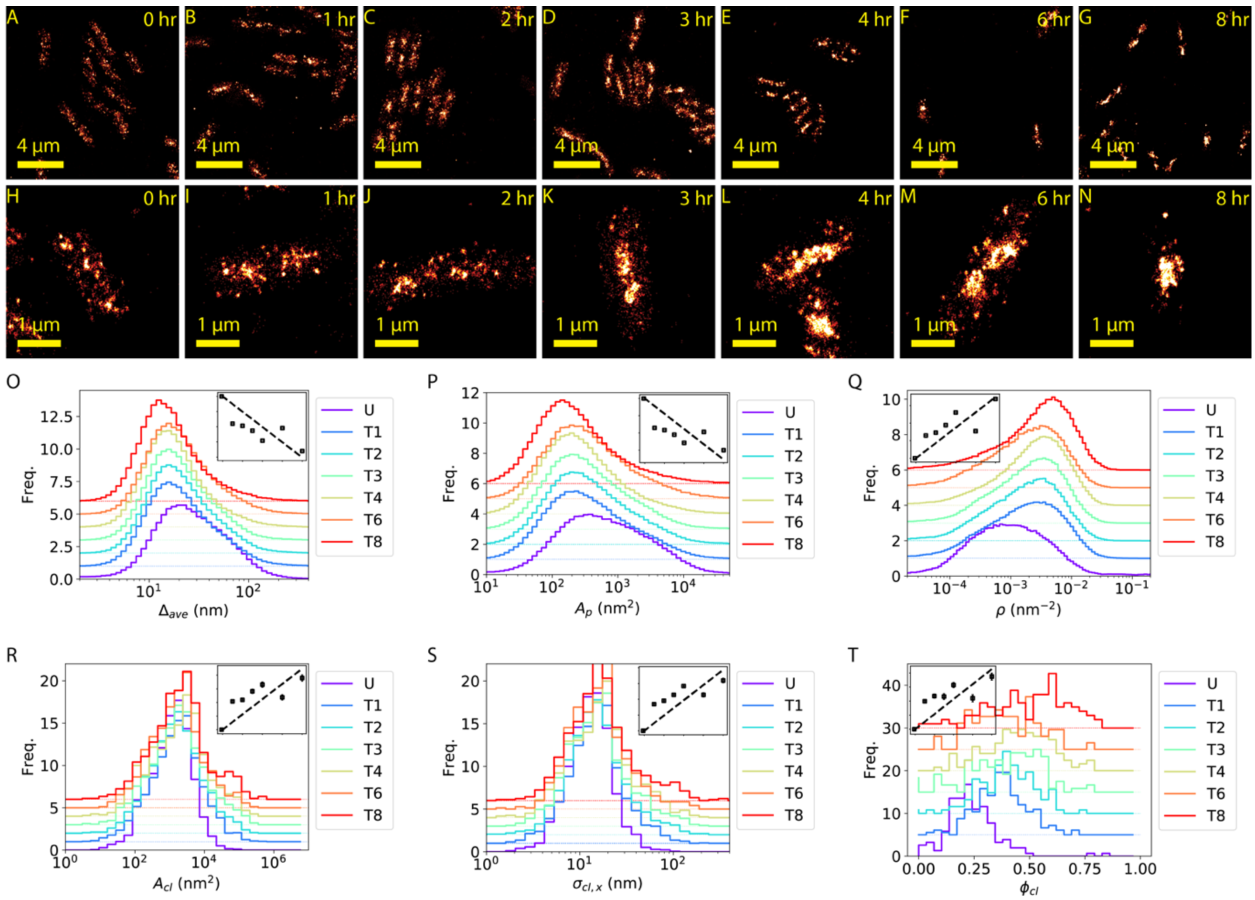

Figure 5. Nanoscale reorganization of H-NS proteins caused by Ag^+ ions. (A-N) Super-resolved images of H-NS proteins in *E. coli* bacteria before (first column) and after (columns 2-8) subjecting bacteria to treatments with Ag^+ ions for 1-8 hours. Panels H-N show zoom-in images of single bacteria. (O-T) Distributions of (O) the mean inter-neighbor distances Δ_{ave}, (P) the molecular area A_p, (Q) the molecular density ρ, (R) the area of clusters A_{cl}, (S) the spread of clusters $\sigma_{cl,x}$, and (T) the clustering fraction ϕ_{cl}. Insets in (O-T) show the dependence of the centers of the distributions (normalized to the untreated bacteria) on treatment-time. Dashed lines are linear fittings.

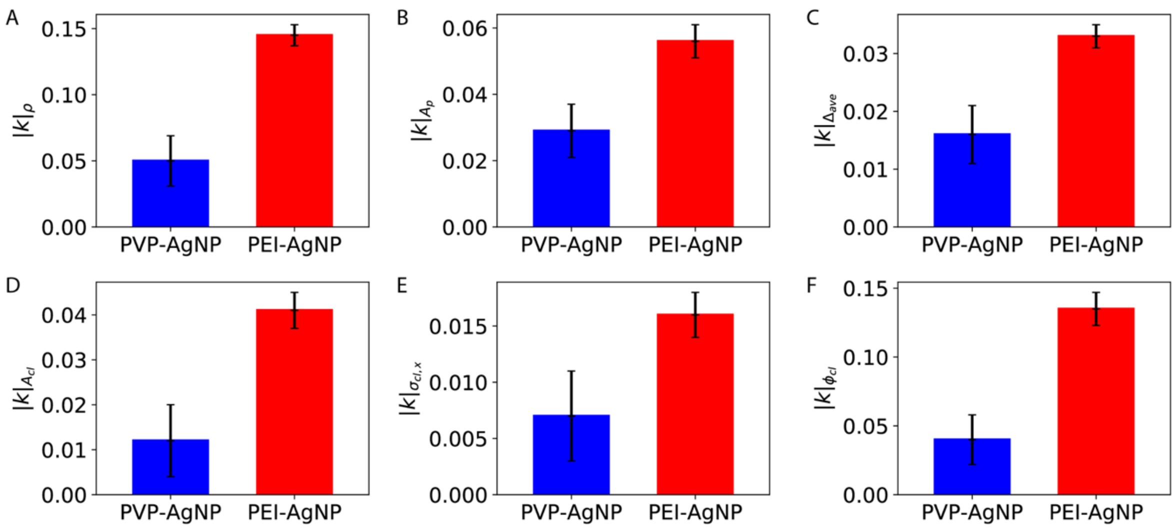

Figure 6. Comparison between PVP-AgNPs and PEI-AgNPs for the changing rates of the dependence of reorganization (i.e., γ's in Fig. 3 and 4) on the treatment time T_{tr}.

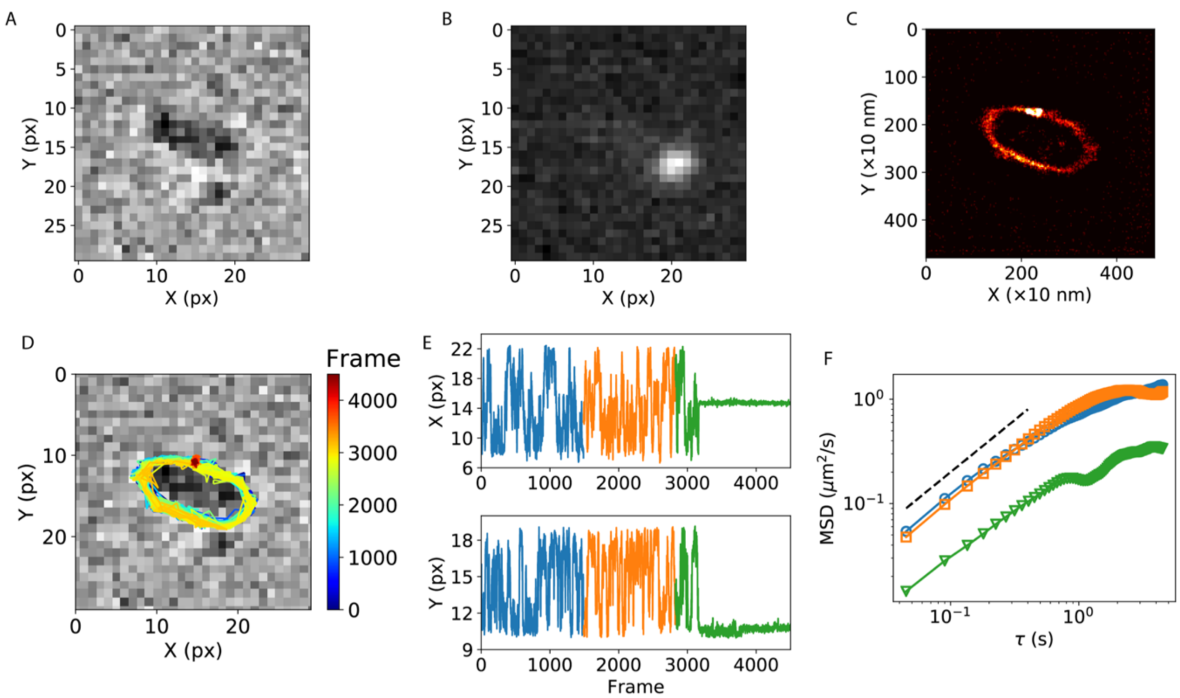

Figure 7. Attachment and dynamic motion of AgNPs on bacterial membrane. (A) A bright-field image of a single bacterium. (B) A conventional fluorescence image of an AgNP attached to the bacterium in panel A. (C) Super-resolved image of the AgNP attached to the bacterium in panel A. (D) Trajectory of the AgNP in the 2D plane, superimposed on the bright-field image. (E) Position of the AgNP as a function of frame number. (F) Mean-square-displacement (MSD) of the three segments of the trajectory of the AgNP in panel E. The dashed line indicates a slope of one.

Supplemental Information

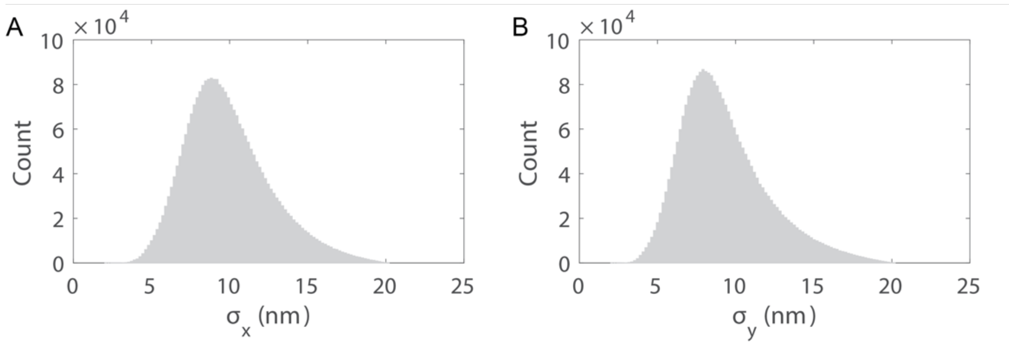

Figure S1. Histograms of the localization precisions, (A) σ_x and (B) σ_y, for our super-resolution fluorescence microscopic data.

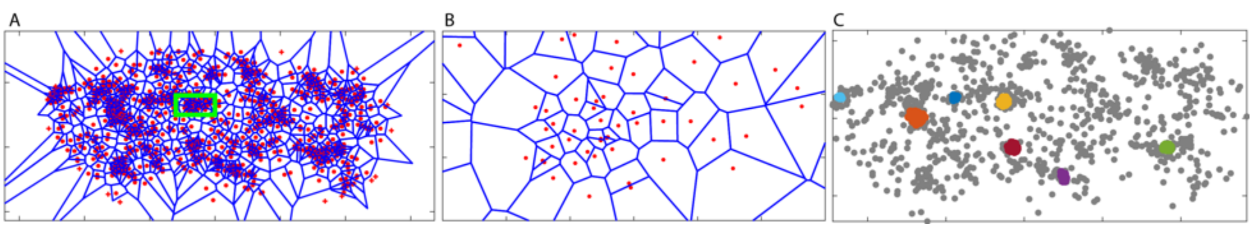

Figure S2. (A) Voronoi diagrams of H-NS proteins in a single bacterium. Red dots represent the H-NS proteins, and blue lines represent edges of Voronoi diagrams. (B) Zoom-in of the green rectangular area in panel A. (C) Identified clusters (colored dots) based on Voronoi diagrams. Gray dots represent non-clustering H-NS proteins.

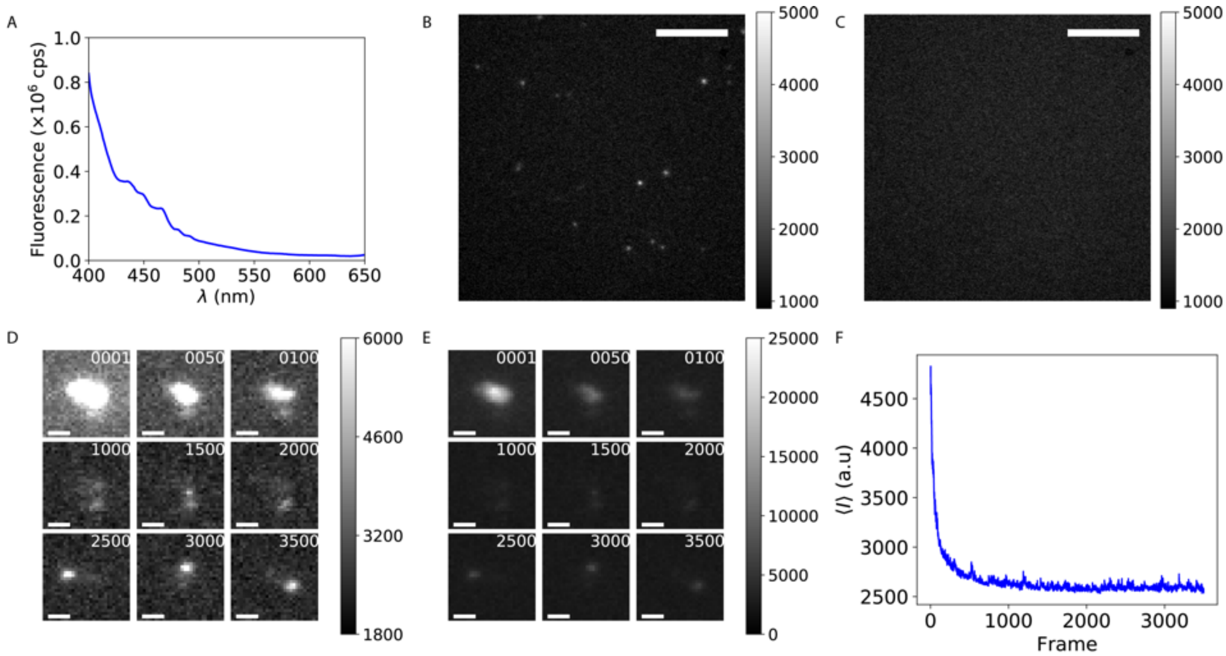

Figure S3. Fluorescence of AgNPs. (A) Fluorescence spectrum of AgNPs excited at 350 nm. (B) Fluorescence image of AgNPs at 40 µg/mL in water immobilized on a coverslip. (C) Fluorescence image of negative control (water without AgNPs). Scale bars in panels B and C are 10 µm. (D, E) Representative frames from a movie of a single bacterium, on which a single AgNP was observed after photobleaching the fluorescent proteins in the bacterium. Panel E is the same data as panel D, except for different color scales. Scale bars in panels D and E are 1 µm. (F) Decrease of the average intensity of the frames due to photobleaching of the fluorescent proteins in the bacterium.

MovieS1.avi (12.5 MB)

Movie S1. Dynamic motion of an AgNP on the bacterial surface.